Single-Atom Chromium-Embedded N-Doped Graphene as a Multifunctional Separator Coating for Lithium–Sulfur Batteries

Frederik Bettels, Donna Rashidi, Zhihua Lin, Leon Schenk, Taoran Li, Haiwei Wu, Irmgard Frank, Ebrahim Nadimi, Yuping Liu,* Chaofeng Zhang, Fei Ding, and Lin Zhang*

Lithium–sulfur (Li–S) batteries offer a promising alternative to traditional lithium-ion batteries due to their high energy density, large capacity, cost advantages, and environmental benefits. However, their commercialization is impeded by challenges like the lithium polysulfide (LiPS) shuttle effect, necessitating advanced sulfur host materials and separator coatings for the effective trapping of LiPSs and enhancing the ion transfer. In this research, single-atom chromium-incorporated nitrogen-doped graphene (Cr@NG) is introduced as a novel separator coating, synthesized by an NaCl soft-template method. This material, as an efficient and economic alternative to other existing single-atom catalysts-based materials, combines high conductivity and catalytic activity, effectively suppressing the shuttle effect and enhancing sulfur conversion. First-principles calculations and electrochemical studies further demonstrate that Cr@NG significantly improves adsorption capabilities, capacity retention, rate capability, and cycling stability. The incorporation of chromium offers substantial benefits in electron transport and catalytic efficiency, establishing Cr@NG as a promising multifunctional separator coating for high-performance Li–S batteries.

1. Introduction

Lithium–sulfur (Li–S) batteries have gained significant attention in recent years due to their high theoretical energy density (2600 Wh kg^{-1}) and high theoretical capacity (1675 mAh g^{-1}).[1] These attributes, coupled with environmental benignity and low cost, give them the potential to surpass traditional lithium-ion batteries.[2] However, practical challenges such as the lithium polysulfide (LiPS) shuttle effect and corrosion of Li metal impede their commercialization.[3] The shuttle effect, driven by the dissolution and migration of LiPSs in the electrolyte during charge-discharge cycles, leads to active material loss and internal self-discharge.[4] Additionally, the low conductivity of elemental sulfur and LiPSs contributes to sluggish electrochemical reaction kinetics and low sulfur utilization, which collectively results in rapid capacity fading and limited cycle life.[5] Addressing these issues requires innovative strategies such as advanced sulfur host materials[6] or separator coatings[7,1a] that can immobilize LiPSs and promote their conversion.

Recent research has highlighted the potential of separator coatings as a viable strategy to inhibit the migration of polysulfides.[8] Separator coatings with carbon-based materials,[9] metal oxides[10] and sulfides[11] have demonstrated improved cycle stability and reduced polysulfide dissolution by acting as physical barriers and offering catalytic sites for LiPS conversion.[12,1a] However, carbon-based materials are usually nonpolar and can only trap LiPSs within their porous structure, leading to irreversible

F. Bettels, Z. Lin, L. Schenk, T. Li, F. Ding, L. Zhang
Institute of Solid State Physics and Laboratory of Nano- and Quantum Engineering
Leibniz University Hannover
30167 Hannover, Germany
E-mail: lin.zhang@fkp.uni-hannover.de

D. Rashidi, E. Nadimi
Center for Computational Micro and Nanoelectronics
Faculty of Electrical Engineering
K. N. Toosi University of Technology
Tehran 16317-14191, Iran

H. Wu
Shaanxi Provincial Key Laboratory of Papermaking Technology and Specialty Paper Development
College of Bioresources Chemical and Materials Engineering
Shaanxi University of Science &Technology
Xi'an 710021, P. R. China

I. Frank
Institute of Physical Chemistry and Electrochemistry
Leibniz University Hannover
30167 Hannover, Germany

Y. Liu
Research Center for Electrochemical Energy Storage Technologies
Chongqing Institute of Green and Intelligent Technology
Chinese Academy of Sciences
Chongqing 400714, P. R. China
E-mail: liuyuping@cigit.ac.cn

C. Zhang
Institutes of Physical Science and Information Technology
Leibniz Joint Research Center of Materials Sciences
Key Laboratory of Structure and Functional Regulation of Hybrid Material (Ministry of Education)
Anhui University
Hefei 230601, P. R. China

deposition of insoluble sulfides.[13] In contrast, most metal oxides and sulfides are semiconductors or even insulators, which decrease the Li+ ion transfer and the interface redox kinetics on the surface.[14]

To overcome these obstacles, functionalized carbon materials like nitrogen-doped graphene (NG) have been recognized for their excellent conductivity and structural robustness.[15] However, NG requires further modification to optimize its performance in Li–S batteries.[3b] In this context, introducing transition metals such as cobalt[16] or nickel[17] into NG as single-atom catalyst (SAC) has demonstrated considerable promise. Recently, Lin et al. developed a cobalt single-atom functional interlayer on nitrogen-doped porous carbon/NG composite (Co$_{SAC}$-NPC/NG), enhancing LiPS adsorption and catalysis. Its porous structure and high conductivity reduces polarization voltage and accelerates polysulfide conversion, achieving 1457.9 mAh g^{-1} at 0.1 C and 788.7 mAh g^{-1} after 400 cycles.[16b] Additionally, Chen et al. synthesized a high-density vanadium SACs (HD-V-SACs) with 13.0 wt% vanadium on nitrogen-doped carbon nanosheets, significantly enhancing LiPS redox kinetics. HD-V-SACs increase the discharge capacity to 1143.9 mAh g^{-1} at 0.5 C and maintain 76.3% retention over 500 cycles, even with high sulfur loading.[8c] These SACs significantly enhance the catalytic properties and interactions with sulfur species, thereby improving the immobilization and conversion of LiPSs.[18] The high surface area and unique electronic properties of SACs enhance their catalytic efficiencies, making them particularly suited for Li–S batteries.[19]

Herein, we introduce single-atom chromium-incorporated NG (Cr@NG) as a novel separator coating synthesized using a NaCl soft-template method. This innovative approach aims to synergize high conductivity and catalytic activity to mitigate the shuttle effect and facilitate sulfur conversion, thereby enhancing the electrochemical capabilities of Li–S batteries. The use of NaCl as a soft template not only provides a simple and environmentally benign route but also ensures uniform dispersion and optimal surface area for catalysis.[20,15b] Compared to previously reported transition metal catalysts, Cr offers a highly cost-effective alternative due to its low price and favorable electrochemical properties. It demonstrates a small free energy change during the discharge process and a low decomposition barrier for Li$_2$S during the charge cycle, indicating that Cr can possibly deliver catalytic performance that is comparable to existing alternatives.[21] Our first-principles calculations reveal insights into the enhanced adsorption capabilities and catalytic behaviors of Cr@NG. The electrochemical performance of Cr@NG is thoroughly evaluated against NG, demonstrating superior rate capability, high capacity retention of 835.8 mAh g^{-1} after 300 cycles at 0.2 C, and cycling stability of 600 cycles at 0.5 C. We detail how the incorporation of Cr significantly enhances these properties, underscoring Cr@NG's potential as an advanced material for high-performance Li–S battery applications.

2. Results and Discussion

2.1. Material Synthesis and Characterization

Cr@NG and NG were synthesized via an NaCl soft-template method (see experimental section),[21] which is depicted in
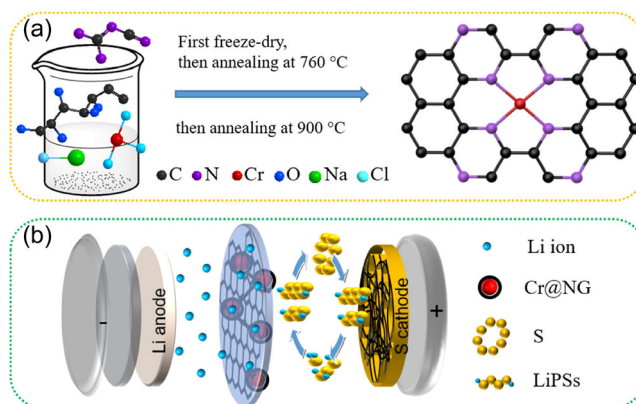
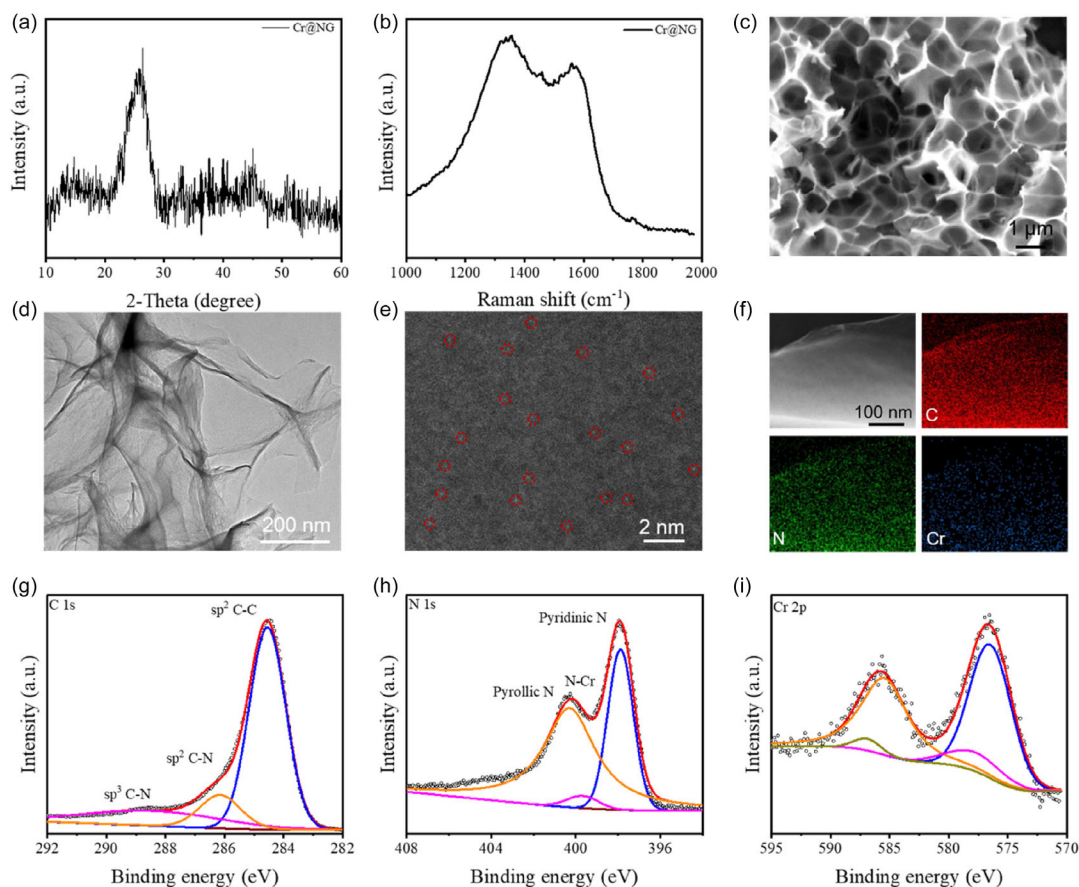

Figure 1. a) Schematic illustration of synthesis process and b) schematic representation of the working principles of the Cr@NG-modified separator in the Li–S battery.

Figure 1a. Briefly, for the synthesis of Cr@NG, NaCl, dicyandiamide, glucose, and chromium chloride hexahydrate were thoroughly mixed in distilled water. The resulting solution was then immediately frozen by liquid nitrogen and freeze-dried for 48 h. Afterwards, the precursor was calcinated at 760 C under N$_2$ atmosphere, followed by removing the NaCl template by washing with distilled water and a subsequent calcination at 900 C under N$_2$ to obtain the final product. Subsequently, the synthesized material is applied as a functional separator coating facing the cathode in Li–S batteries Figure 1b.[21]

To analyze the structure of the synthesized materials, XRD measurements and Raman spectroscopy were conducted. The XRD measurement of Cr@NG (**Figure 2**a) reveals a strong and broad peak at 26°, corresponding to the (002) plane, and a weak peak at 45°, corresponding to the (100) plane of graphene derivatives. The broadening of these peaks can be attributed to N defects within the graphene structure.[22] Compared to NG, no additional signals are observed, suggesting the presence of single-atom Cr (Figure S1, Supporting Information). Figure 2b displays the Raman spectrum for Cr@NG that shows the characteristic D band at 1350 cm^{-1} and G band at 1570 cm^{-1}, typical for graphene derivatives. The intensity ratio I_D/I_G is ≈1.19 for Cr@NG, indicating a high level of structural defects within the graphene structure originated from N-doping and Cr incorporation into the honeycomb lattice of graphene. NG exhibits a similar spectrum (Figure S2, Supporting Information).[23]

For the investigation of the morphology and the composition of the synthesized catalyst material, we conducted scanning electron microscopy (SEM), energy-dispersive X-ray spectroscopy (EDXS), and transmission electron microscopy (TEM). The SEM image (Figure 2c) and TEM image (Figure 2d) reveal the porous and interconnected flake-like structure for Cr@NG. The abundant pores in Cr@NG can provide larger contact interface, expose more active sites, and facilitates electron and ion transport.[24,19b] Additionally, there are no Cr metal clusters or nanoparticles observed, indicating the good dispersion of Cr atoms in the NG structure.

To reveal the atomic-level structure of Cr@NG, high-angle annular dark field–scanning TEM (HAADF-STEM) was performed. The HAADF-STEM images show monodispersed Cr single-atoms

Batteries & Supercaps

Research Article
doi.org/10.1002/batt.202500200

Chemistry Europe
European Chemical
Societies Publishing

Figure 2. Morphological and structural characterization of Cr@NG. a) XRD, b) Raman spectroscopy, c) SEM image, d) TEM image, e) HAADF-STEM image, f) corresponding elemental mapping, and XPS analysis of the g) C 1 s, h) N 1 s, and i) Cr 2p spectrum.

(bright spots encircled in red in Figure 2e) in the NG framework. This characteristic is essential for attaining highly efficient catalysis at the atomic level.[19a] To verify the compositional structure, EDXS measurements were performed, showing a uniform distribution of C, N, and Cr within Cr@NG (Figure 2f). Additionally, the loading of Cr is determined to 2 at. % (Figure S3, Supporting Information). For comparison, NG is also investigated, showing a similar morphology like Cr@NG without the presence of Cr (Figures S5–8, Supporting Information).

To analyze the compositional and chemical structure of Cr@NG, high-resolution X-ray photoelectron spectroscopy (XPS) was performed as shown in Figure 2g–i. The C 1 s spectrum shows a major peak at 284.55 eV assigned to the sp^2 C—C bond, the two additional peaks at 286.15 and 288.44 eV are associated with the sp^2 C—N and sp^3 C—N bonds, respectively, confirming the successful doping with nitrogen. The two peaks in the N 1 s spectrum at 397.89 and 400.29 eV correspond to pyrrolic-N and pyridinic-N, respectively. Additionally, the peak at 399.68 eV can be assigned to the N 1 s signal of the N—Cr bond.[25] The Cr 2p spectrum shows a spin-orbit doublet at 576.63 and 585.61 eV for Cr $2p_{3/2}$ and Cr $2p_{1/2}$ which is assigned to a Cr(II) oxidation, and another at 577.8 and 586.9 eV corresponding to Cr(III) oxidation. No additional peaks corresponding to chromium oxide or zero-valent Cr are observed, further indicating the successful synthesis of SACs.[26] For comparison, the XPS spectra of NG are displayed in Figure
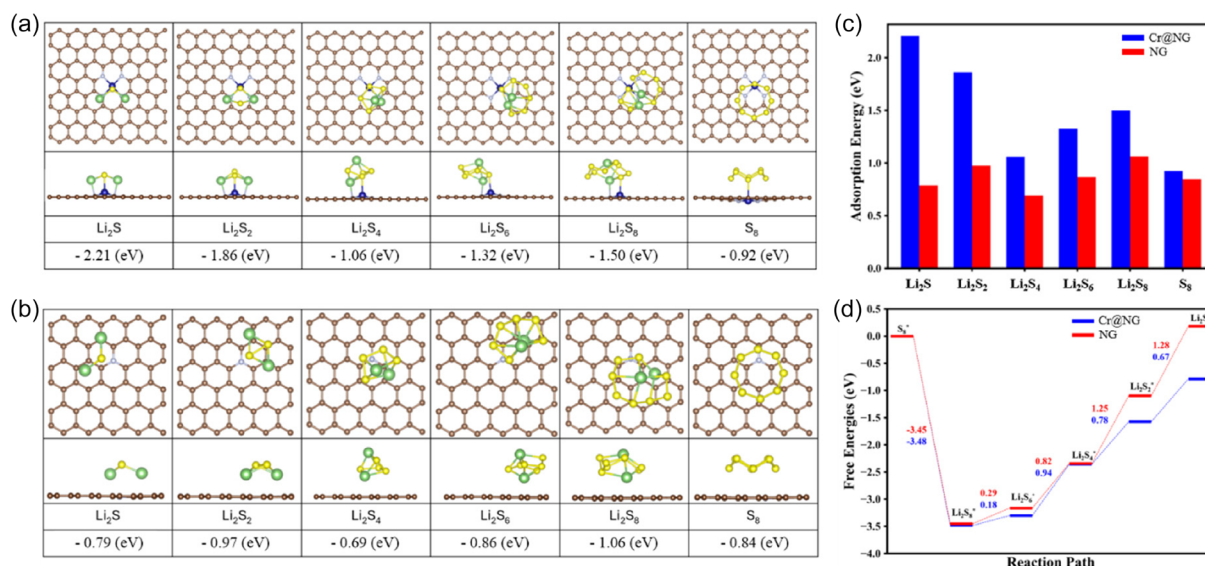
S8, Supporting Information, showing that the C 1 s and N 1 s data are similar but without the presence of Cr.

2.2. Reaction Mechanism of Cr@NG

To gain a deeper understanding of the chemical interactions between LiPSs and Cr@NG, we conducted first-principles calculations. Initially, the formation energy for coordination of a Cr atom with four pyridinic-N atoms is calculated to be −2.35 eV (Figure S9, Supporting Information). This negative formation energy indicates that the formation of Cr@NG is exothermic and thermodynamically stable, suggesting that it can occur spontaneously under the given conditions.[27] Our findings are corroborated by our XPS measurements and align with existing literature, confirming the stability and feasibility of this coordination structure.[20,21]

Figure 3a presents the two most stable models of NG, both with and without Cr atom, as modeled in the simulation. The Cr atom is marked in dark blue, Li in green, S in yellow, and N in light blue. For suppressing the shuttle effect, trapping and immobilization of LiPSs are essential. Therefore, we calculated the adsorption energy to have insights into the interaction between Cr@NG or NG and LiPSs/ elemental sulfur (S_8) and to unravel the role of Cr. The adsorption energies for NG with respect to S_8, Li_2S_8, Li_2S_6, Li_2S_4, Li_2S_2, and Li_2S are −0.84, −1.06, −0.86, −0.69, −0.97,

Batteries & Supercaps

Research Article
doi.org/10.1002/batt.202500200

Chemistry
Europe
European Chemical
Societies Publishing

Figure 3. Energy profiles for LiPSs on Cr@NG and NG. a) Optimized atomic structures and corresponding adsorption energies of LiPSs on Cr@NG obtained from first-principles calculations, b) optimized atomic structures and corresponding adsorption energies of LiPSs on NG obtained from first-principles calculations, c) comparison of calculated adsorption energies of LiPSs on Cr@NG and NG, respectively, and d) comparison of energy profiles of the LiPSs reduction on Cr@NG and NG, respectively.

and -0.79 eV, respectively. Here, a more negative value indicates stronger adsorption.

In contrast, Cr@NG shows greatly improved adsorption capabilities of -0.92, -1.5, -1.32, -1.06, -1.86, and -2.21 eV, respectively. In comparison, the adsorption energies for Cr@NG are substantially higher than in the case of NG (Figure 3b). The improved adsorption results from the almost parallel binding of LiPSs to Cr@NG and the binding of Li and S with N and Cr in Cr@NG, respectively. Especially, the formation of a Cr—S bond is due to the ability of Cr to form stable covalent interactions with S. These bonds effectively stabilize LiPSs, enhancing their adsorption and preventing migration. Additionally, Cr—S bonds promote efficient electron transfer between LiPSs and Cr@NG and enable catalytic conversion of polysulfides, ensuring improved rate capability and increased sulfur utilization.[21,25]
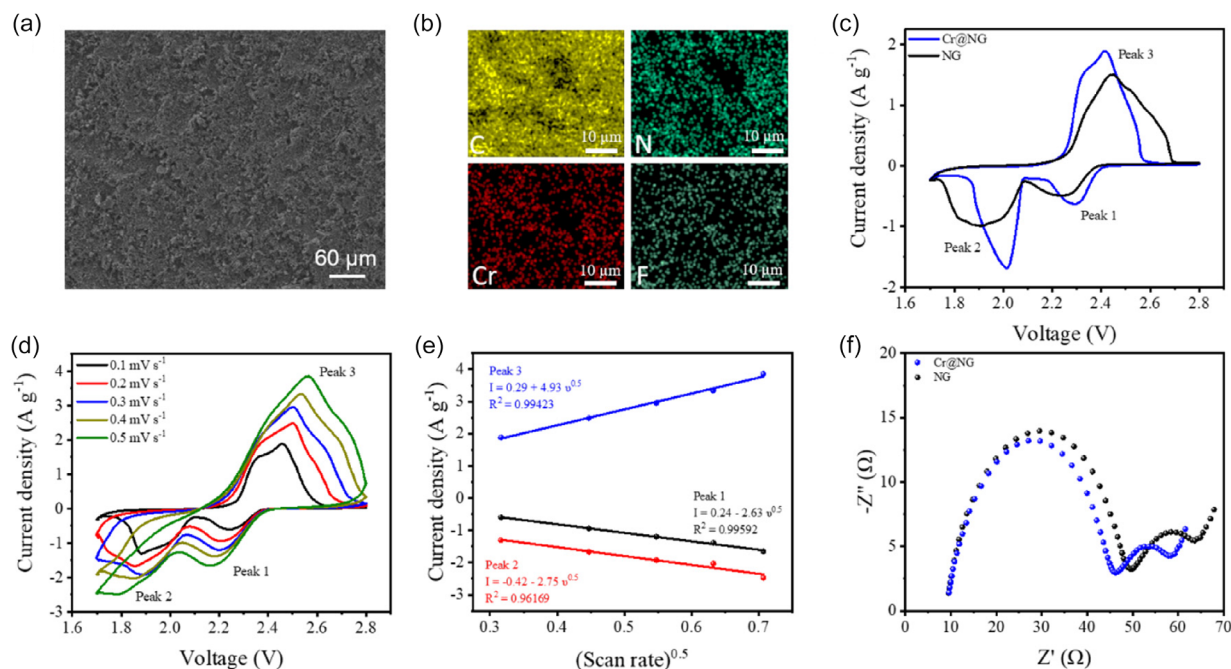
Subsequently, the reduction pathways of sulfur for both Cr@NG and NG were investigated, focusing on the complete reversible conversion of Li and S_8 into Li_2S. Initially, S_8 undergoes a stepwise reduction, where it is doubly reduced by two Li^+ ions to form Li_2S_8. This is followed by successive reduction of Li_2S_8 leading to the formation of three intermediate LiPSs: Li_2S_6, Li_2S_4, and Li_2S_2, and finally ending with the formation of Li_2S. The Gibbs free energies were calculated for the above reactions for both Cr@NG and NG and are displayed in Figure 3c. After the spontaneous exothermic reaction of S_8 to Li_2S_8, the formation of intermediate LiPSs and Li_2S are either endothermic or nearly thermoneutral. The formation of Li_2S_4 from Li_2S_6 is found to be the rate-limiting step in the whole discharge process for Cr@NG, as it has the highest Gibbs free energy with 0.94 eV. In contrast, the limiting steps of NG are the conversions from Li_2S_4 to Li_2S with a free energy of 1.25 and 1.28 eV, respectively. The comparison with the free energies

of Cr@NG, 0.78 and 0.67 eV, indicates an acceleration of the reaction kinetics for short-chain LiPSs by the catalytic characteristics of Cr@NG. In total, the first-principles calculations show higher adsorption of LiPSs leading to immobilization and the promotion of conversion by Cr@NG, which results in hindering the shuttle effect and, consequently, in an improvement of battery performance.

2.3. Electrochemical Performance

Encouraged by the theoretical results, we investigated the chemical interaction and electrocatalytic behavior of Cr@NG with polysulfides. Using symmetric cells assembled with Cr@NG electrodes and a Li_2S_6 catholyte, cyclic voltammetry (CV) was performed at a scan rate of 0.2 mV s^{-1} over a voltage range of -1.0 to 1.0 V. In Figure S10, Supporting Information, the CV profile of Cr@NG reveals prominent peaks corresponding to the redox conversion of LiPSs. During the cathodic scan, peaks at 0.10 V (peak 1) and -0.29 V (peak 2) indicate the reduction of S_8 to Li_2S_6 and Li_2S_6 to Li_2S_2/Li_2S, respectively. The anodic scan presents peaks at -0.09 V (peak 3) and 0.28 V (peak 4), corresponding to the oxidation of Li_2S_2/Li_2S to Li_2S_6 and then to S_8. In contrast, the CV scan of NG shows only one reduction peak at -0.33 V and one oxidation peak at 0.33 V, indicating lower catalytic activity. The smaller potential separation between anodic and cathodic peaks and the higher current response of Cr@NG demonstrate enhanced redox kinetics and reduced polarization, confirming its superior catalytic efficiency in polysulfide conversion.[28]

To further investigate the electrochemical behavior of the synthesized materials, Cr@NG or NG is mixed with carbon black (CB) and PVDF and then subsequently coated on a commercial Celgard 2400 separator. The catalyst loading is determined to be 0.226 mg cm^{-2}. The electrode consisted of nanosulfur, CB,

Batteries & Supercaps

Research Article
doi.org/10.1002/batt.202500200

Chemistry Europe
European Chemical
Societies Publishing

Figure 4. Electrocatalytic analysis of Cr@NG. a) SEM images of Cr@NG coated separator, b) EDXS of Cr@NG coated separator, c) CV curves of Cr@NG and NG at 0.1 mV s^{-1} (second cycle), d) CV curves of Cr@NG at different scan rates, e) linear relationship between peak current density and square root of scan rates, and f) EIS.
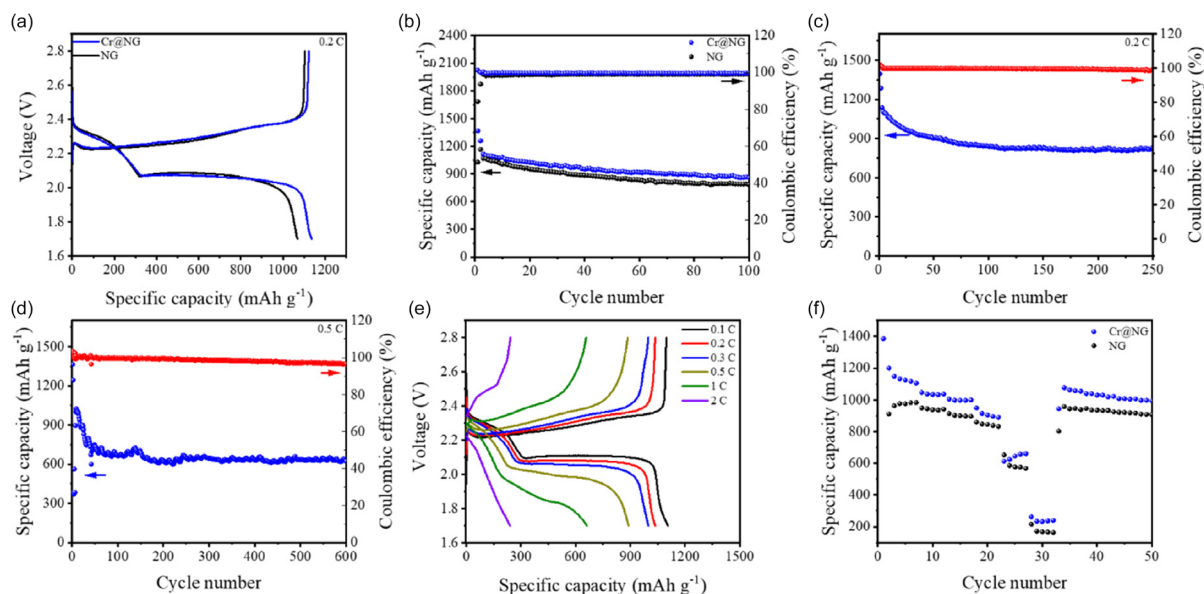
EC, and PVDF in a ratio 6:2:1:1 coated onto Al foil. The SEM image (**Figure 4**a) displays the uniform coating of the Cr@NG. The corresponding EDXS measurement shows a uniform distribution of C, N, Cr, and F within the matrix (Figure 4b). The CV analysis (Figure 4c) reveals two distinctive pairs of oxidation and reduction peaks for both Cr@NG and NG. The cathodic peaks correspond to the reduction of S$_8$ to soluble long-chain LiPSs and the conversion to solid Li$_2$S. Conversely, the anodic peaks represent the oxidation of Li$_2$S via LiPSs to S$_8$. In comparison, Cr@NG exhibited higher current densities, sharper peaks and lower overpotentials between oxidation and reduction peaks compared to NG (Figure S11, Supporting Information), indicating superior electron transport and catalytic activity. These characteristics manifest the suppression of polysulfide shuttling and improved catalysis, leading to more rapid and efficient redox reactions, thus enhancing overall battery performance. Importantly, no extraneous peaks related to side reactions in the electrolyte were observed in the CV scans.

Figure S12, Supporting Information, illustrates the reversibility of the redox reaction of LiPSs achieved by the Cr@NG coated separator, evidenced by the overlapping CV curves over three cycles. Additionally, the Li$^+$ diffusion coefficient (D) is an important parameter, which influences the performance of the battery, particularly in the context of the LIPSs formation during charge and discharge. For its investigation, CV measurements at different scan rates were performed for both Cr@NG and NG (Figure 4d and Figure S13a, Supporting Information). D is determined by using the Randles–Sevcik equation[29] (1) where I_P is the peak current density, n is the the number of electrons transferred in the redox reaction, A is the electrode area, F is the Faraday constant, C_{Li} is the concentration of Li* ions in the electrolyte, R is the gas constant, T is the temperature and v is the scan rate.

$$I_P = 0.4463 \ n^{1.5}F^{1.5}AC_{Li}D^{0.5}(RT)^{-0.5}v^{0.5} \tag{1}$$

For each peak, I_P is plotted against $v^{0.5}$, showing a linear relationship (Figure 4e and Figure S13b, Supporting Information). Finally, D is calculated from the slope of the linear fit for each peak with n equal to two, $C_{Li} = 0.00129$ mol cm^{-3} based on the electrolyte and a separator area of 2.835 cm^2. For Cr@NG the D are 6.46×10^{-6}, 7.07×10^{-6} and 2.27×10^{-5} cm^2 s^{-1}, respectively, whereas for NG, 5.38×10^{-6}, and 2.81×10^{-5} cm^2 s^{-1}, respectively. The second peak vanishes at higher scan rates for NG. In comparison, Cr@NG demonstrates higher diffusion coefficients for the reduction reaction, suggesting more efficient kinetics for reduction of higher-order LiPSs to lower-order LiPSs or Li$_2$S. In contrast, NG shows a slightly higher diffusion coefficient for the oxidation reaction, indicating improved oxidation kinetics.[30]

To gain more insight into the battery, electrochemical impedance spectroscopy (EIS) is conducted (Figure 4f). The Nyquist curves of Cr@NG and NG show, besides the characteristic first semicircle, a second semicircle originated from the LiPSs dissolution into the electrolyte since the electrode is not modified for hindering. In comparison with NG, Cr@NG exhibits a lower series resistance (R$_S$) of 8.13 Ω, for NG R$_S$ is 9.53 Ω, suggesting a decrease in the separator resistance due to the incorporation of Cr single-atoms. Moreover, the width of the first semicircle represents the charge transfer resistance R$_{ct1}$ relating to reaction kinetics and interfacial properties. Cr@NG demonstrates an R$_{ct1}$ of 36.71 Ω, in contrary NG exhibits 40.16 Ω. This reduction in resistance suggests improved reaction kinetics in Cr@NG, which is consistent with our theoretical calculations. The second semicircle relates to the charge transfer resistance (R$_{ct2}$) at the sulfur cathode, especially involving sulfur conversion reactions like polysulfide formation and Li$_2$S deposition. Cr@NG

Batteries & Supercaps

Research Article
doi.org/10.1002/batt.202500200

Chemistry Europe
European Chemical
Societies Publishing

Figure 5. Electrochemical performance of Cr@NG and NG coated separator. a) charge/discharge profile of Cr@NG and NG at 0.2 C, b) cycling performance of Cr@NG and NG at 0.2 C, c) long-term stability of Cr@NG at 0.2 C, d) long-term stability of Cr@NG at 0.5 C, e) charge/discharge profiles of Cr@NG at different C rates, and f) rate performance of Cr@NG and NG.

exhibits an R_{ct2} of 11.54 Ω compared to 13.95 Ω of NG, indicating better management of polysulfide migration and enhancement of active material utilization.[31]

Further evaluation of battery performance was conducted by galvanostatic discharge/charge and rate capability tests. Initially, batteries perform two activation cycles at 0.05 C before testing. **Figure 5**a displays the first voltage profile at 0.2 C. Albeit, NG shows a slightly smaller polarization than Cr@NG, Cr@NG exhibits still a higher initial discharge capacity of 1136.4 mAh g^{-1} compared to 1069 mAh g^{-1} of NG. The cycling performance (Figure 5b) clarifies the achievement of implementing Cr into the NG structure. After 100 cycles at 0.2 C, Cr@NG exhibits a high specific capacity of 860.3 mAh g^{-1} whereas NG only features 788.1 mAh g^{-1}. Even after 250 cycles at 0.2 C, Cr@NG still has a capacity of 824.1 mAh g^{-1} with a capacity loss per cycle of 0.11% (Figure 5c).

Figure 5d displays the cycling performance of Cr@NG at high C rate of 0.5 C. After eight activation cycles with low specific capacity, Cr@NG shows a high specific capacity of 1026 mAh g^{-1} with remaining 623.6 mAh g^{-1} after 600 cycles and a capacity loss per cycle of 0.06%. The improvement in longevity and reduced capacity fading can be attributed to the suppression of the shuttling effect and enhancement of catalytic activity of Cr@NG, as revealed by first-principles calculations.

At higher sulfur loadings of ≈2 mg cm^{-2}, both materials, Cr@NG and NG, require an extended activation phase of 6 and 7 cycles, respectively, to achieve specific capacities comparable to those observed at lower sulfur loadings (Figure S14, Supporting Information). After 50 cycles, Cr@NG maintains a specific capacity of 968.4 mAh g^{-1} whereas NG delivers only 939.8 mAh g^{-1}. The rate capabilities of Cr@NG were measured under current densities from 0.1 to 2 C (Figure 5e,d). The reversible capacities observed were 1105.7, 1036.4, 999.1, 889.8, 660.9, and 239.8 mAh g^{-1} for

rates of 0.1, 0.2, 0.3, 0.5, 1, and 2 C, respectively. After returning to 0.2 C, the capacity recovered to a high value, confirming an excellent reversibility. NG shows capacities of 983.5, 941.4, 898.8, 832.4, 567.9, and 163.4 mAh g^{-1} for the same rates. In comparison, Cr@NG exhibits superior rate performance over NG, attributed to the effectiveness of Cr as an electrocatalyst enhancing the electron transport dynamics.

3. Conclusion

In summary, incorporating single-atom Cr into NG using a NaCl soft-template method significantly improves the electrochemical performance of Li–S batteries. Morphological analysis confirms a uniform and porous structure, while XPS and EDXS verify successful N-doping and Cr incorporation. First-principles calculations show that Cr enhances adsorption, helping to trap and stabilize LiPSs while accelerating their conversion, effectively suppressing the shuttle effect. Electrochemical tests demonstrate that Cr@NG delivers superior rate performance, a higher initial capacity (1136.4 mAh g^{-1} at 0.2 C), and better cycling stability compared to NG. The presence of Cr improves electron transport and catalytic activity, enabling more efficient redox reactions and extending battery lifespan. These findings establish Cr@NG as a promising material for high-performance Li–S batteries.

4. Experimental Section

Materials

Sodium chloride (NaCl), dicyandiamide, glucose, lithium sulfide, and chromium chloride hexahydrate were purchased from Sigma–Aldrich (Germany). Nanosulfur, PVDF, CB (SuperP), and ketjen black (EC) were

Batteries & Supercaps

Research Article
doi.org/10.1002/batt.202500200

Chemistry
Europe

European Chemical
Societies Publishing

purchased from Nanografi (Turkey). All chemicals were used without further purification.

Cr@NG Synthesis and Separator Coating

For synthesizing Cr@NG, 8.5 g NaCl, 1.2 g dicyandiamide, 0.62 g glucose, and 34.93 mg chromium chloride hexahydrate were mixed in 75 mL distilled water. The mixture was immediately frozen using liquid nitrogen and subsequently freeze-dried for 48 h. Then, the precursor was annealed to 760 °C for 2 h with a heating rate of 4 °C min^{-1} under nitrogen protection. After cooling to room temperature, the sample was washed in distilled water and dried at 60 °C in an oven. In the final step, the precursor was annealed to 900 °C for 1 h (heating rate 5 C min^{-1}) under nitrogen protection to obtain the final product. For comparison, NG was synthesized without the addition of metal salt. The separator coating was prepared by dry mixing the catalyst material with CB and PVDF (ratio of 8:1:1) in a mortar, then, NMP was added to form a slurry, which was uniformly coated by a coating bar on a commercial Celgard 2400 membrane and dried at 60 °C under vacuum overnight. Finally, the separator was punched into 19 mm diameter pieces.

Materials Characterization

The morphology, microstructure, and composition was characterized by a scanning electron microscope (Raith Pioneer Two) with an EDXS system (Bruker QUANTAX 200), transmission electron microscope (FEI TEM Tecnai G2 F20 TMP operated at 200 kV), and HAADF-STEM (JEOL NeoARM operated at 200 kV). XPS analysis was conducted by PHI Versaprobe III Scanning ESCA. Raman spectroscopy was conducted by Horiba XploRA Plus V1.2, and XRD was conducted by Bruker D8 Advance.

First-Principles Calculations

In this work, all calculations were carried out using spin-polarized density functional theory with the SIESTA software package.[32] The electronic wave functions were represented using a double-zeta plus polarization set of numerical atomic orbitals. In addition, norm-conserving pseudopotentials were utilized to represent the interaction between core and valence electrons. The exchange-correlation interactions were estimated using the Perdew–Burke–Ernzerhof (PBE) functional within the framework of the generalized gradient approximation.[33] To accurately capture dispersion interactions among octasulfur (S_8), lithium polysulfides (Li_2S_x, where $x = 8$, 6, 4, 2, 1), NG and Cr@NG, a van der Waals (vdW) correction was applied to the Perdew–Burke–Ernzerhof (PBE) functional.[34] A mesh cutoff energy of 200 Ry was set to ensure accurate real-space grid resolution. In addition, $4 \times 4 \times 1$ and $2 \times 2 \times 1$ Monkhorst-Pack k-point grids were employed to sample the Brillouin zone efficiently for the supercell of NG and Cr@NG, respectively. Using the conjugate gradient algorithm, atomic positions were optimized until the force on each atom fell below 0.01 eV Å^{-1}. To avoid boundary interactions, a vacuum spacing of 20 Å was applied in the vertical direction of the periodic supercell. The formation energy was computed based on the following formula

$$E_f = E_{Cr@NG} - E_G + m\mu_c - \left(\frac{n}{2}\mu_n + \mu_{Cr}\right) \qquad (2)$$

This equation defines $E_{Cr@NG}$ as the total energy of the Cr@NG system and E_G as the total energy of the original system without Cr@NG, where E_G specifically represents the initial energy of pristine graphene. The chemical potentials μ_i (where $i = $ C, N, Cr) were obtained from pristine graphene, N_2 gas molecule, and Cr in its standard state.

The adsorption energy E_{ads} was calculated as

$$E_{ads} = E_{molecule+host} - E_{molecule} - E_{host} + \delta_{BSSE} \qquad (3)$$

where $E_{molecule+host}$, $E_{molecule}$ and E_{host} denotes the energies of S_8 and the Li_2S_x molecules, NG and Cr@NG as the host material, and the adsorption system. δ_{BSSE} represents the basis set superposition error (BSSE).

The variations in Gibbs free energy for the reduction steps are described by the following equations

$$\Delta G_1 = G(^*Li_2S_8) - G(^*S_8) - 2G(Li) \qquad (4)$$

$$\Delta G_2 = G(^*Li_2S_6) + 2G(S) - G(^*Li_2S_8) \qquad (5)$$

$$\Delta G_3 = G(^*Li_2S_4) + 2G(S) - G(^*Li_2S_6) \qquad (6)$$

$$\Delta G_4 = G(^*Li_2S_2) + 2G(S) - G(^*Li_2S_4) \qquad (7)$$

$$\Delta G_5 = G(^*Li_2S) + G(S) - G(^*Li_2S_2) \qquad (8)$$

Electrochemical Measurements

The sulfur electrodes were prepared by mixing nanosulfur, CB, EC, and PVDF in a ratio of 6:2:1:1 with NMP to form a slurry. This slurry was uniformly coated onto Al foil and dried under vacuum at 60 C overnight. The dried material was then punched into pieces with a diameter of 12 mm. The sulfur loading was $\approx$1.3 mg cm^{-2}. For evaluating the electrochemical performance, CR2032 cells were assembled with a sulfur electrode as cathode, lithium foil as anode, the coated membrane as separator, and 1M LiTFSI in DOL/DME (volume ratio 1:1) with 2 % of LiNO$_3$ additive as electrolyte. The electrolyte/sulfur ratio was $\approx$28 μL mg^{-1}. Galvanostatic discharge/charge measurements were performed with a LAND CT 2001 A charge/discharge system in a voltage range of 1.7–2.8 V. The CV curves were conducted by Metrohm Autolab at scan rates of 0.1–0.5 mV s^{-1} in a voltage range of 1.7–2.8 V. The EIS was also measured by Metrohm Autolab in the frequency range from 100 kHz to 10 mHz with 10 mV amplitude. For symmetric cells, a 0.2 M Li$_2$S$_6$ catholyte was prepared by dissolving S and Li$_2$S (5:1 molar ratio) in the electrolyte and vigorous stirring for 24 h. For the electrodes, Cr@NG or NG was mixed with PVDF in a ratio of 9:1 in NMP to form a slurry. This slurry was uniformly coated onto Al foil and dried under vacuum at 60 C overnight. The dried electrode was then punched into pieces with a diameter of 12 mm. Two identical electrodes are assembled to a coin cell with addition of 40 μL of Li$_2$S$_6$ catholyte and a Celgard 2400 membrane as separator. The CV curves were conducted by Metrohm Autolab at scan rate of 0.2 mV s^{-1} in a voltage range of −1.0–1.0 V.

Batteries & Supercaps

Research Article
doi.org/10.1002/batt.202500200

Chemistry Europe
European Chemical
Societies Publishing

Conflict of Interest

The authors declare no conflict of interest.

Author Contributions

Lin Zhang conceived and supervised the project. **Frederik Bettels** designed and performed the experiments, analysis, and interpretation of data. **Donna Rashidi** and **Ebrahim Nadimi** performed and analyzed the first-principles calculations. **Zhihua Lin**, **Leon Schenk**, **Taoran Li**, and **Haiwei Wu** assisted in laboratory management. **Irmgard Frank**, **Ebrahim Nadimi**, **Yuping Liu**, **Chaofeng Zhang**, **Fei Ding** and **Lin Zhang** revised the manuscript.

Data Availability Statement

The data that support the findings of this study are available in the supplementary material of this article.

[1] a) M. Waqas, Y. Niu, M. Tang, Y. Pang, S. Ali, Y. Dong, W. Lv, W. He, *Energy Storage Mater.* **2024**, *72*, 103682; b) R. Kumar, J. Liu, J. Y. Hwang, Y. K. Sun, *J. Mater. Chem. A.* **2018**, *6*, 11582.

[2] a) P. G. Bruce, S. A. Freunberger, L. J. Hardwick, J. M. Tarascon, *Nature Mater.* **2012**, *11*, 19; b) A. Rosenman, E. Markevich, G. Salitra, D. Aurbach, A. Garsuch, F. F. Chesneau, *Adv. Energy Mater.* **2015**, *5*, 1500212.

[3] a) W. Kang, N. Deng, J. Ju, Q. Li, D. Wu, X. Ma, L. Li, M. Naebe, B. Cheng, *Nanoscale* **2016**, *8*, 16541; b) Y. Liu, A. Chatterjee, P. Rusch, C. Wu, P. Nan, M. Peng, F. Bettels, T. Li, C. Ma, C. Zhang, B. Ge, N. C. Bigall, H. Pfnür, F. Ding, L. Zhang, *ACS Nano* **2021**, *15*, 15047; c) K. Xu, *Chem. Rev.* **2004**, *104*, 4303.

[4] a) Z. W. Seh, Y. Sun, Q. Zhang, Y. Cui, *Chem. Soc. Rev.* **2016**, *45*, 5605; b) S. Gu, C. Sun, D. Xu, Y. Lu, J. Jin, Z. Wen, *Electrochem. Energy Rev.* **2018**, *1*, 599; c) Y. Liu, Y. Barnscheidt, M. Peng, F. Bettels, T. Li, T. He, F. Ding, L. Zhang, *Adv. Sci.* **2021**, *8*, 2101182.

[5] a) H. Raza, S. Bai, J. Cheng, S. Majumder, H. Zhu, Q. Liu, X. Li, G. Chen, *Electrochem. Energy Rev.* **2023**, *6*, 29; b) A. Manthiram, Y. Fu, Y. S. Su, *Acc. Chem. Res.* **2013**, *46*, 1125.

[6] a) Q. Pang, X. Liang, C. Y. Kwok, L. F. Nazar, *Nat. Energy* **2016**, *1*, 1; b) K. Fan, H. Huang, *Energy Storage Mater.* **2022**, *50*, 696; c) Y. Liu, S. Ma, L. Liu, J. Koch, M. Rosebrock, T. Li, F. Bettels, T. He, H. Pfnür, N. C. Bigall, A. Feldhoff, F. Ding, L. Zhang, *Adv. Funct. Mater.* **2020**, *30*, 2002462.

[7] Y. Wang, R. Ai, F. Wang, X. Hu, Y. Zeng, J. Hou, J. Zhao, Y. Zhang, Y. Zhang, X. Li, *Polymers* **2023**, *15*, 993.

[8] a) X. Huang, R. He, M. Li, M. O. L. Chee, P. Dong, J. Lu, *Mater. Today* **2020**, *41*, 143; b) D. Son, W. G. Lim, J. Lee, *Korean J. Chem. Eng.* **2023**, *40*, 473; c) Q. Chen, J. Si, H. Huang, W. Wang, W. Zhang, S. Meng, L. Liu, *J. Mater. Chem. A* **2025**, *13*, 16958.

[9] a) J. Balach, T. Jaumann, M. Klose, S. Oswald, J. Eckert, L. Giebeler, *Adv. Funct. Mater.* **2015**, *25*, 5285; b) J. Cai, Y. Song, X. Chen, Z. Sun, Y. Yi, J. Sun, Q. Zhang, *J. Mater. Chem. A* **2020**, *8*, 1757.

[10] a) Z. Li, C. Zhou, J. Hua, X. Hong, C. Sun, H. W. Li, X. Xu, L. Mai, *Adv. Mater.* **2020**, *32*, 1907444; b) J. Wu, Q. Feng, Y. Wang, J. Wang, X. Zhao, L. Zhan, M. Liu, Z. Jin, Z. Chen, Y. Lei, *Chem. Commun.* **2023**, *59*, 2966.

[11] Z. A. Ghazi, X. He, A. M. Khattak, N. A. Khan, B. Liang, A. Iqbal, J. Wang, H. Sin, L. Li, Z. Tang, *Adv. Mater.* **2017**, *29*, 1606817.

[12] Y. Xiang, J. Li, J. Lei, D. Liu, Z. Xie, D. Qu, K. Li, T. Deng, H. Tang, *ChemSusChem* **2016**, *9*, 3023.

[13] H. Shi, W. Lv, C. Zhang, D. W. Wang, G. Ling, Y. He, F. Kang, Q. H. Yang, *Adv. Funct. Mater.* **2018**, *28*, 1800508.

[14] Z. Zhang, J. N. Wang, A. H. Shao, D. G. Xiong, J. W. Liu, C. Y. Lao, K. Yi, S. Y. Lu, Q. Jiang, J. Yu, H. L. Li, Z. Y. Yang, R. V. Kumar, *Sci. China Mater* **2020**, *63*, 2443.

[15] a) Y. Qiu, W. Li, W. Zhao, G. Li, Y. Hou, M. Liu, L. Zhou, F. Ye, H. Li, Z. Wei, S. Yang, W. Duan, Y. Ye, J. Guo, Y. Zhang, *Nano Lett.* **2014**, *14*, 4821; b) N. Wei, L. Yu, Z. Sun, Y. Song, M. Wang, Z. Tian, Y. Xia, J. Cai, Y.-Y. Li, L. Zhao, Q. Li, M. H. Rümmeli, J. Sun, Z. Liu, *ACS Nano*, **2019**, *13*, 7517.

[16] a) Z. Du, X. Chen, W. Hu, C. Chuang, S. Xie, A. Hu, W. Yan, X. Kong, H. Ji, L. J. Wan, *J. Am. Chem. Soc.* **2019**, *141*, 3977; b) F. J. Lin, C. L. Huang, X. Y. Jiang, J. Q. Liao, Y. Y. Li, *ACS Sustainable Chem. Eng.* **2024**, *12*, 3478.

[17] a) L. Zhang, D. Liu, Z. Muhammad, F. Wan, W. Xie, Y. Wang, L. Song, Z. Niu, J. Chen, *Adv. Mater.* **2019**, *31*, 1903955; b) K. Zhang, Z. Chen, R. Ning, S. Xi, W. Tang, Y. Du, C. Liu, Z. Ren, X. Chi, M. Bai, C. Shen, X. Li, X. Wang, X. Zhao, K. Leng, S. J. Pennycook, H. Li, H. Xu, K. P. Loh, K. Xie, *ACS Appl. Mater. Interfaces* **2019**, *11*, 25147.

[18] a) J. Xi, H. S. Jung, Y. Xu, F. Xiao, J. W. Bae, S. Wang, *Adv. Funct. Mater.* **2021**, *31*, 2008318; b) Z. Liang, J. Shen, X. Xu, F. Li, J. Liu, B. Yuan, Y. Yu, M. Zhu, *Adv. Mater.* **2022**, *34*, 2200102.

[19] a) S. K. Kaiser, Z. Chen, D. Faust Akl, S. Mitchell, J. Pérez-Ramírez, *Chem. Rev.* **2020**, *120*, 11703, b) T. Zhou, J. Liang, S. Ye, Q. Zhang, J. Liu, *Energy Storage Mater.* **2023**, *55*, 322.

[20] Z. Yang, Y. Dang, P. Zhai, Y. Wei, Q. Chen, J. Zuo, X. Gu, Y. Yao, X. Wang, F. Zhao, J. Wang, S. Yang, P. Tang, Y. Gong, *Adv. Energy Mater.* **2022**, *12*, 2103368.

[21] X. Han, Z. Zhang, X. Xu, *J. Mater. Chem. A* **2021**, *9*, 12225.

[22] C. Wang, J. Kang, H. Sun, H. M. Ang, M. O. Tadé, S. Wang, *Carbon* **2016**, *102*, 279.

[23] Y. Shang, H. Xu, M. Li, G. Zhang, *Nano* **2017**, *12*, 1750018.

[24] Y. Jiang, Y. Deng, B. Zhang, W. Hua, X. Wang, Q. Qi, Q. Lin, W. Lv, *Nanoscale* **2020**, *12*, 12308.

[25] Z. Li, P. Li, Z. Huang, D. Wang, D. Ma, L. Zheng, S. Lu, Q. Yue, *Chem. Eng. J.* **2024**, *496*, 153642.

[26] F. Chen, X. L. Wu, C. Shi, H. Lin, J. Chen, Y. Shi, S. Wang, X. Duan, *Adv. Funct. Mater.* **2021**, *31*, 2007877.

[27] a) W. Yang, M. Zhao, X. Ding, K. Ma, C. Wu, I. D. Gates, Z. Gao, *Phys. Chem. Chem. Phys.* **2020**, *22*, 3983; b) B. An, J. Zhou, Z. Zhu, Y. Li, L. Wang, J. Zhang, *Fuel* **2022**, *310*, 122472.

[28] a) K. Sun, Y. Fu, T. Sekine, H. Mabuchi, S. Hossain, Q. Zhang, D. Liu, S. Das, D. He, Y. Negishi, *Small* **2024**, *20*, 2304210, b) Y. Li, J. Xu, D. Xu, Y. He, X. Sun, D. Niu, X. Zhang, *ChemElectroChem* **2021**, *8*, 1642.

[29] X. Huang, Z. Wang, R. Knibbe, B. Luo, S. A. Ahad, D. Sun, L. Wang, *Energy Technol.* **2019**, *7*, 1801001.

[30] R. Wang, J. Yang, X. Chen, Y. Zhao, W. Zhao, G. Qian, S. Li, Y. Xiao, H. Chen, Y. Ye, G. Zhou, F. Pan, *Adv. Energy Mater.* **2020**, *10*, 1903550.

[31] M. Geng, H. Yang, C. Shang, *Adv. Sci.* **2022**, *9*, 2204561.

[32] J. M. Soler, E. Artacho, J. D. Gale, A. García, J. Junquera, P. Ordejón, D. Sánchez-Portal, *J. Phys.: Condens. Matter* **2002**, *14*, 2745.

[33] P. Perdew, K. Burke, M. Ernzerhof, *Phys. Rev. Lett.* **1996**, *77*, 3865.

[34] M. Dion, H. Rydberg, E. Schröder, D. C. Langreth, B. I. Lundqvist, *Phys. Rev. Lett.* **2004**, *92*, 246401.